Microbubble detection using Neyman-Pearson theory for volumetric ultrasound localization microscopy

Valentin Mazellier, Georges Chabouh, Olivier Couture, Pauline Muleki Seya, François Varray

▶ **To cite this version:**

Valentin Mazellier, Georges Chabouh, Olivier Couture, Pauline Muleki Seya, François Varray. Microbubble detection using Neyman-Pearson theory for volumetric ultrasound localization microscopy. 2024 Ultrasonics, Ferroelectrics, and Frequency Control Joint Symposium, Sep 2024, Taipei, Taiwan. hal-04762252

HAL Id: hal-04762252
https://hal.science/hal-04762252v1

Submitted on 4 Nov 2024

HAL is a multi-disciplinary open access archive for the deposit and dissemination of scientific research documents, whether they are published or not. The documents may come from teaching and research institutions in France or abroad, or from public or private research centers.

L'archive ouverte pluridisciplinaire **HAL**, est destinée au dépôt et à la diffusion de documents scientifiques de niveau recherche, publiés ou non, émanant des établissements d'enseignement et de recherche français ou étrangers, des laboratoires publics ou privés.

Microbubble detection using Neyman-Pearson theory for volumetric ultrasound localization microscopy

1st Valentin Mazellier
CREATIS Laboratory
CNRS, UCBL1, INSA, INSERM
Villeurbanne, France
valentin.mazellier@creatis.insa-lyon.fr

2rd George Chabouh
Laboratoire d'Imagerie Biomédicale
INSERM, CNRS, Sorbonne university
Paris, France
georges.chabouh@sorbonne-universite.fr

3th Olivier Couture
Laboratoire d'Imagerie Biomédicale
INSERM, CNRS, Sorbonne university
Paris, France
olivier.couture@sorbonne-universite.fr

4nd Pauline Muleki-Seya
CREATIS Laboratory
CNRS, UCBL1, INSA, INSERM
Villeurbanne, France
pauline.muleki-seya@creatis.insa-lyon.fr

5th François Varray
CREATIS Laboratory
CNRS, UCBL1, INSA, INSERM
Villeurbanne, France
francois.varray@creatis.insa-lyon.fr

***Abstract*—Microbubble (MB) identification is a crucial step in ultrasound localization microscopy (ULM) as it defines the patches of clutter-filtered brightness (B-mode) images where the sub-wavelength localization algorithm should be applied. Neyman-Pearson (NP) criterion has been applied as a method for MB detection in 2D *in-vivo* ULM. The principle of NP is to establish a pixel-specific threshold based on the pixel's temporal statistics. NP increased the resolution compared to intensity based identification (INT) and had a more complete mapping of the vessels than cross-correlation based identification (COR). However, the previously proposed method was limited to 2D and suffered from the out-of-plane motion and from the inability to capture the 3D structure of vascularization. Herein, NP is first extended to volumetric imaging and then compared to 3D INT and 3D COR. Simulation results demonstrate that the proposed method is more effective in detecting the low signal-to-noise ratio MBs compared to INT. *In vivo* rat kidney data further reveal that NP produces fewer artifacts in ULM maps while achieving similar resolution to INT and COR. In the other hand, NP produced less blurry maps, which may indicate either that NP detects less noise or that it is less sensitive to MBs.**

***Index Terms*—Ultrasound localization microscopy, Super-resolution, Neyman-Pearson, 3D imaging, microbubble detection**

I. Introduction

Ultrasound localization microscopy (ULM) allows to map vessels with a resolution beyond the diffraction limit, [1], [2], [3]. The pipeline of Ultrasound ULM consists of multiple steps, each crucial for achieving high-resolution vascular imaging. Ongoing research focuses on optimizing these individual steps to further enhance the accuracy and detail of the vascular representations produced by ULM. Microbubble (MB) detection occurs after clutter filtering: This process identify the MB signature within the filtered data, thereby enabling the utilization of the sub-wavelength localization algorithm. An efficient MB identifier is of prior importance for two reasons: (i) false MB identifications can create artifacts on the final ULM map, and (ii) missing MBs will increase the time needed to obtain a good representation of the vessel network.

Several MB identification methods have been developed, two of which will be employed for comparison with NP. The first one is directly based on the intensity of pixels (INT), [4]. It assumes that after filtering, the n first local maxima are produced by MBs, with n a number empirically chosen. INT is very sensitive to noise and can fail to discriminate residual tissue signals of high intensity from MBs. The second widely used method is based on the cross-correlation (COR) of the filtered B-mode images with an MB point spread function (PSF). This PSF can be measured, simulated, or approximated with a Gaussian kernel. INT and COR are sometimes used together for better results [5]. COR has good performances but will fail when the PSF shape varies with space or because of overlapping MBs. Deep-learning-based methods are also in development. An example comes from [6], who correlates the filtered images with a PSF, and afterwards, a 3D CNN transforms the correlation map into tracks. This approach eliminates the need to choose which correlation peaks represent MBs but still relies on the COR method.

To tackle those problems, a new MB identifier has been developed recently by [7]. It increased the resolution on *in vivo* data compared to INT and provided a more complete reconstruction of the vascularization than COR. It uses decision theory and the Neyman-Pearson criterion (NP) to define an intensity threshold specific to each pixel based on its time statistics. However, its implementation was limited to 2D ULM. It suffered from out-of-plane motion and was not able to capture the 3D structure of the vessels.

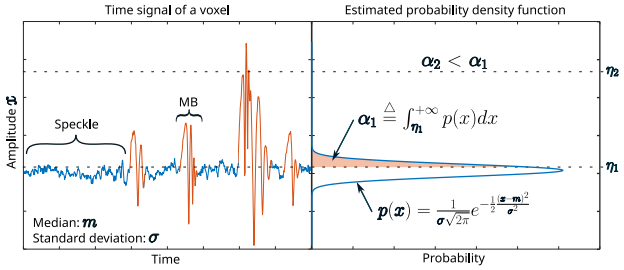

Fig. 1. (Left) Time signal from a voxel with speckle in blue and microbubbles in orange. (Right) The probability density function approximated as a Gaussian and Neyman-pearson criterion to define the microbubble intensity threshold η. Effect of α on η is showed with two examples: α_1 and α_2.

This work extends NP to 3D ULM and will try to answer whether NP should be used over COR and INT for volumetric ULM. In this purpose, the methods are compared regarding precision and recall on simulations. Then *in vivo* externalized rat kidney data [8] are used for qualitative analysis.

II. Identification methods

A. Neyman-Pearson

In vivo temporal signal from a single voxel $\mathbf{r}$ after clutter filtering is illustrated on Fig. 1 (left). The remaining clutter signal is shown in blue, while the MB signal is depicted in orange. It can be seen that MBs have different amplitudes when passing by this voxel. These amplitude variations are even more pronounced across different voxels. This variability complicates the application of a single intensity threshold across the entire volume. The NP approach addresses this by computing a voxel-specific threshold based on the temporal statistics of each voxel.

The first step of the proposed method is to define two hypotheses:

- H_0: Signal comes from speckle only.
- H_1: Signal comes from speckle and MB.

The objective is now to find the threshold η such that

$$x_{\mathbf{r}}(t) \underset{H_0}{\overset{H_1}{\gtrless}} \eta \ , \tag{1}$$

with $x_{\mathbf{r}}(t)$ the amplitude of voxel at the instant t. The meaning of (1) is: "If $x_{\mathbf{r}}(t)$ is higher than η, an MB is then detected."

The Neyman-Pearson theory offers a methodology for determining the threshold η. This requires the specification of a false alarm rate, $\alpha \in [0;1]$. It quantifies the tolerance to false detections in this context. This parameter is linked to η by

$$\alpha \triangleq \int_{\eta}^{+\infty} p(x_{\mathbf{r}}(t)|H_0)dx \ , \tag{2}$$

where p is the probability density function (PDF). The PDF of a single voxel can be approximated as a Gaussian:

$$p(x_{\mathbf{r}}(t)|H_0) = \frac{1}{\sigma\sqrt{2\pi}} e^{-\frac{1}{2}\frac{(x_{\mathbf{r}}-m)^2}{\sigma^2}} \ . \tag{3}$$

The mean m and the standard deviation σ are computed on $x_{\mathbf{r}}(t)$ using respectively the median and the median absolute deviation for more robustness to noise. By injecting equation (3) in equation (2), it is possible to isolate η. The decision rule (1) finally becomes:

$$x_{i,j,k}(t) \underset{H_0}{\overset{H_1}{\gtrless}} \sigma\sqrt{2}\mathrm{erf}^{-1}(1-2\alpha) + m \triangleq \eta \ . \tag{4}$$

with erf^{-1} the inverse error function. For more detailed calculus, please refer to [7]. In equation (2), α is defined solely based on the H_0 hypothesis. However, the distinction between the signal components corresponding to H_0 and H_1 is unknown in practice. Consequently, experimental estimates for m and σ are derived from the entire signal rather than exclusively from the speckle component.

The right side of Fig. 1 illustrates the impact of α on the NP threshold. All MBs are detected for a high value of $\alpha = \alpha_1$. However, some speckle components are also incorrectly classified and belong to H_1. On the other hand, when α is reduced to α_2, speckle is no longer detected, but several MBs are missed. The user is responsible for determining the α value that best fits the data. To mitigate the effects of a high α, only the n highest local maxima after thresholding are considered as MBs.

B. Intensity- and correlation-based methods

The two other MB identification methods used in this study for comparison are INT and COR. In the first case, the Matlab function *imregionalmax* is applied to the volume to find the local maxima. The first n maxima are then kept and considered as MBs. It is a straightforward method that heavily depends on the number n defined by the user. Furthermore, this method can detect high intensity noise and miss low intensity MBs. In the latter method a PSF is simulated with a 3D Gaussian kernel. For a voxel size of half a wavelength, the standard deviation of the Gaussian is 2. A normalized cross-correlation is then done between the PSF and the volume. Voxels with a correlation under a threshold τ_{ncc} are set 0 and the first n local maxima of the correlation map are considered as MBs. This method needs two parameters to be defined: τ_{ncc} and n.

III. Simulation study

A. Simulation

The 3D simulator described in [9] was employed to generate the spatial positions of 50 MBs per volume across 400 volumes. This simulator exploits the vascular network of a mouse brain acquired via two-photon microscopy to produce realistic MB trajectories and velocities. Initially, the network has dimensions of $0.5 \times 0.5 \times 0.65$ mm, then is expanded to a volume of $8.1 \times 8.1 \times 12$ mm. With the MB positions established, the MUST toolbox [10] was used to simulate radiofrequency (RF) data from a 1024-element matrix probe with a central frequency of 8 MHz. An experimental speckle, acquired with the same probe on a phantom with hand

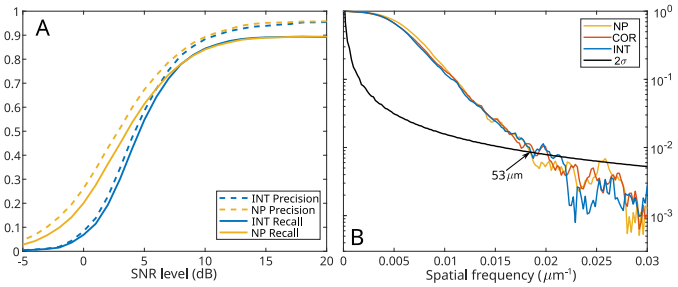

Fig. 2. Metrics comparison: **(A)** Precision and recall of NP and INT on simulated data. **(B)** FSC of *in vivo* data with a grid size of 9.9 μm

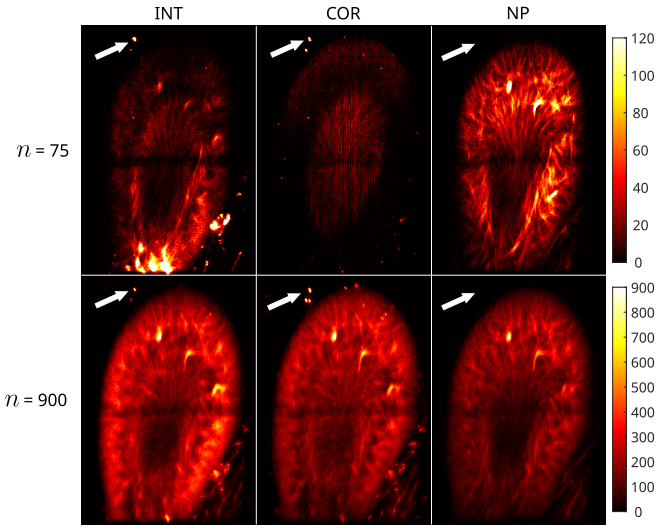

Fig. 3. Microbubble per pixel map obtained using either INT, COR, or NP based microbubbles identification. Maps are summed along the elevation dimension. The grid resolution is 16 μm. (First line) Results with n = 75 local maxima. (Second line) The n = 900 local maxima. An example of the artifact is marked with a white arrow.

movement, was subsequently added to the simulated post-beamforming data. The signal-to-noise ratio (SNR) between MBs and speckle varies between -5 dB and 20 dB by step of 1 dB.

B. Results

Two metrics are computed: precision and recall. The first corresponds the ratio between the number of true detections and the total number of detections. The second metric, recall, is the ratio between the number of true detections with the number of MBs in all the volumes. A detection is considered true when an MB position is located less than a quarter of the wavelength from it. For this application α is set to 0.1 and $n = 50$. Fig. 2A shows metrics for the different SNR levels.

For high SNR values, INT and NP exhibit similar performances. However, as the SNR decreases, NP begins to outperform INT. The maximum gain is observed at an SNR of 2 dB, where NP shows an increase of 0.2 and 0.17 in precision and recall compared to INT. COR curves are not displayed as it did not provide satisfactory results. Speckle sometimes exhibits PSF-like patterns that trick the detection, which explains COR's poor metrics. This experiment demonstrates that NP is superior to INT for detecting MBs at low SNR on simulated data.

IV. *In vivo* STUDY

In vivo data comes from the study [8]. It consists of 500 blocks of 200 volumes acquired on an externalized rat kidney. The same matrix probe as in the simulation study was used. Volumes were clutter filtered using a singular value decomposition. For the ULM exploitation, all steps are identical except for the MB identification method. An Hungarian algorithm from *simpletracker* toolbox is used for tracking followed by sub-wavelength localization conducted with 3D radial symmetry [11]. The maximum linking distance is set to 3 voxels (= 295 μm), and tracks shorter than 18 temporal steps are removed. For this application, α and τ_{ncc} are empirically set to 0.01 and 0.6, respectively. Fig. 3 shows the ULM density map with the three different MB identification methods on a grid 6 times smaller than the original (= 16 μm). Volumes are summed along the elevation axis for display. A dark line can be seen in all images. The energy of the filtered volumes

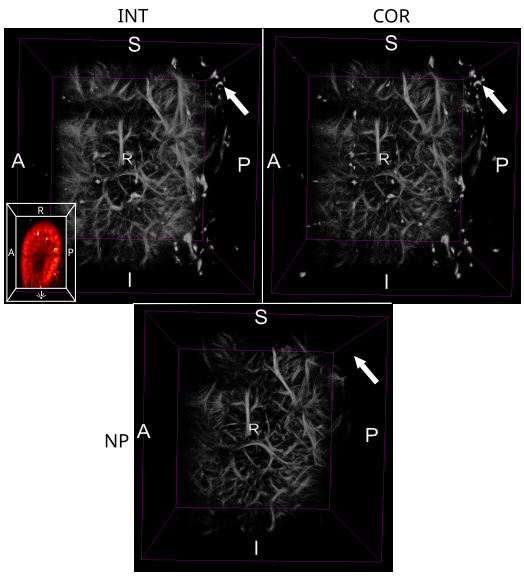

Fig. 4. 3D representation of INT, COR, and NP microbubble per voxel maps with a 9.9 μm grid size. An example of an artifact is highlighted with a white arrow.

is lower in this area which results in a lower probability of detecting MBs.

The first line of Fig. 3 corresponds to results with $n = 75$. It appears that NP visually has the best representation of vessels. COR reconstructed fewer tracks than INT or NP resulting in the worst ULM map of the three. Additionally, COR and particularly INT maps display artifacts that NP avoided. An example of the artifact is marked with a white arrow in Fig. 3. In the second line the number of local maxima n retained is raised to 900. By doing so, the risk of detecting noise is increased, but fewer MBs should be

missed. This time, all methods have a good representation of vessels. However, NP still shows no artifacts, while the ones from INT and COR have increased.
Fig. 4 is a 3D representation of the same maps with $n = 900$. This display helps to see the numerous artifacts avoided by NP. For example, the white arrow marks an artifact hidden in Fig. 3. It is notable that certain regions of the volume are less blurry with COR and are even clearer with NP, compared to INT. This blur is created by voxels with low MB density, which are challenging to interpret. These voxels may represent vessels with very few MBs passage or could be caused by noise. Two conclusions can be drawn from this observation: either COR, and especially NP, identify less MBs compared to INT, or COR, and particularly INT, are detecting more noise than NP.

The Fourier shell Correlation (FSC) is computed on a grid 10 times smaller than the original ($= 9.9$ μm). The high intensities and sharp edges of artifacts create high spatial frequencies and false results. To avoid this effect, FSC is computed in a region of interest without artifacts. In Fig. 2B, the resulting curves are smoothed with a moving average of 6 samples. The resolution estimated using the 2σ threshold is 53 μm for all three methods.

V. Conclusion

In this study, we extended a MB identification method based on Neyman-Pearson criterion from 2D to 3D and compared it to traditional methods based on intensity and normalized cross-correlation with a PSF. Simulation results demonstrated that the NP criterion is more effective at detecting low SNR MBs than INT. However, due to the PSF-like patterns present in the speckle, we were unable to assess the performance of the COR method using this data. Qualitative evaluations were conducted using *in vivo* rat kidney acquisitions. NP successfully reconstructed the vascular network even with a small number of local maxima per volume, whereas INT and COR produced false detections, leading to artifacts in the final ULM map. Furthermore, COR reconstructed few tracks and had the worst vessel representation. For a high number of local maxima per volume, all methods provided a good representation of vessels with a resolution of 53 μm . However, INT and COR exhibited artifacts that NP avoided. The ULM map generated by INT was found to be more blurry than those generated by COR and NP. This may indicate that INT detects more noise than COR and NP, or alternatively, that the latter two methods fail to identify certain MBs detected by INT. All three methods are highly sensitive to their respective parameters, which were selected empirically to yield the best results according to the authors' subjective assessment. It is important to note that the observations made in this study are influenced by the specific tuning of these parameters. In conclusion, NP's exploiting temporal information to establish a specific threshold at each voxel enables the reconstruction of more accurate ULM maps with fewer artifacts. Thus, NP may offer a superior alternative to INT and COR, even though these methods yielded satisfactory results.

References

[1] C. Errico, J. Pierre, S. Pezet, Y. Desailly, Z. Lenkei, O. Couture, and M. Tanter, "Ultrafast ultrasound localization microscopy for deep super-resolution vascular imaging," *Nature*, vol. 527, pp. 499–502, Nov. 2015.

[2] O. Couture, V. Hingot, B. Heiles, P. Muleki-Seya, and M. Tanter, "Ultrasound Localization Microscopy and Super-Resolution: A State of the Art," *IEEE Transactions on Ultrasonics, Ferroelectrics, and Frequency Control*, vol. 65, pp. 1304–1320, Aug. 2018.

[3] K. Christensen-Jeffries, O. Couture, P. A. Dayton, Y. C. Eldar, K. Hynynen, F. Kiessling, M. O'Reilly, G. F. Pinton, G. Schmitz, M.-X. Tang, M. Tanter, and R. J. van Sloun, "Super-resolution Ultrasound Imaging," *Ultrasound in Medicine & Biology*, vol. 46, pp. 865–891, Apr. 2020.

[4] B. Heiles, A. Chavignon, V. Hingot, P. Lopez, E. Teston, and O. Couture, "Performance benchmarking of microbubble-localization algorithms for ultrasound localization microscopy," *Nature Biomedical Engineering*, vol. 6, pp. 605–616, Feb. 2022.

[5] B. Heiles, M. Correia, V. Hingot, M. Pernot, J. Provost, M. Tanter, and O. Couture, "Ultrafast 3D Ultrasound Localization Microscopy Using a 32 $\times$ 32 Matrix Array," *IEEE Transactions on Medical Imaging*, vol. 38, pp. 2005–2015, Sept. 2019.

[6] L. Milecki, J. Poree, H. Belgharbi, C. Bourquin, R. Damseh, P. Delafontaine-Martel, F. Lesage, M. Gasse, and J. Provost, "A Deep Learning Framework for Spatiotemporal Ultrasound Localization Microscopy," *IEEE Transactions on Medical Imaging*, vol. 40, pp. 1428–1437, May 2021.

[7] A. Corazza, P. Muleki-Seya, A. Basarab, and B. Nicolas, "Microbubble Identification Based on Decision Theory for Ultrasound Localization Microscopy," *IEEE Open Journal of Ultrasonics, Ferroelectrics, and Frequency Control*, vol. 3, pp. 41–55, 2023.

[8] G. Chabouh, L. Denis, S. Bodard, F. Lager, G. Renault, A. Chavignon, and O. Couture, "Whole organ volumetric sensing Ultrasound Localization Microscopy for characterization of kidney structure," *IEEE Transactions on Medical Imaging*, pp. 1–1, 2024.

[9] H. Belgharbi, J. Porée, R. Damseh, V. Perrot, L. Milecki, P. Delafontaine-Martel, F. Lesage, and J. Provost, "An Anatomically Realistic Simulation Framework for 3D Ultrasound Localization Microscopy," vol. 3, 2023.

[10] D. Garcia and F. Varray, "SIMUS3: An open-source simulator for 3-D ultrasound imaging," *Computer Methods and Programs in Biomedicine*, vol. 250, p. 108169, June 2024.

[11] S.-L. Liu, J. Li, Z.-L. Zhang, Z.-G. Wang, Z.-Q. Tian, G.-P. Wang, and D.-W. Pang, "Fast and High-Accuracy Localization for Three-Dimensional Single-Particle Tracking," *SCIENTIFIC REPORTS*.